Pergamon

Ocean Engineering 26 (1999) 595–623

OCEAN ENGINEERING

An analytic solution to the wave bottom boundary layer governing equation under arbitrary wave forcing

Diane L. Foster[a,*], Ronald A. Guenther[b], Robert A. Holman[c]

[a]*Department of Oceanography, Dalhousie University, Halifax, Nova Scotia, Canada*
[b]*Department of Mathematics, Oregon State University, Corvallis, Oregon, USA*
[c]*College of Oceanic and Atmospheric Sciences, Oregon State University, Corvallis, Oregon, USA*

Received 30 September 1997; accepted 3 December 1997

Abstract

Existing models of the wave bottom boundary layer have focused on the vertical and temporal dynamics associated with monochromatic forcing. While these models have made significant advances, they do not address the more complicated dynamics of random wave forcing, commonly found in natural environments such as the surf zone. In the closed form solution presented here, the eddy viscosity is assumed to vary temporally with the bed shear velocity and linearly with depth, however, the solution technique is valid for any eddy viscosity which is separable in time and space. A transformation of the cross-shore velocity to a distorted spatial domain leads to time-independent boundary conditions, allowing for the derivation of an analytic expression for the temporal and vertical structure of the cross-shore velocity under an arbitrary wave field. The model is compared with two independent laboratory observations. Model calculations of the bed shear velocity are in good agreement with laboratory measurements made by Jonsson and Carlsen (1976, J. Hydraul. Res., 14, 45–60). A variety of monochromatic, skewed, and asymmetric wave forcing conditions, characteristic of those found in the surf zone, are used to evaluate the relative effects on the bed shear. Because the temporal variation of the eddy viscosity is assumed proportional to the bottom shear, a weakly nonlinear interaction is created, and a fraction of the input monochromatic wave energy is transferred to the odd harmonics. For a monochromatic input wave, the ratio of the third harmonic of velocity at the bed to the first is $< 10\%$. However, for a skewed and asymmetric input wave, this ratio can be as large as 30% and is shown to increase with increasing root-mean-square input wave acceleration. The work done by the fluid on the bed is shown to be a maximum under purely skewed waves and is directed onshore. Under purely asymmetric waves, the

* Corresponding author

PII: S0029-8018(98)00016-X

work done is significantly smaller and directed offshore.

Keywords: Wave bottom boundary layer; Arbitrary wave forcing

1. Introduction

The region of fluid near a boundary is termed the boundary layer and has been the subject of much research over this past century. The importance of the boundary layer has been recognized in fields ranging from aeronautical engineering to oceanography. In wave dominated coastal environments, the wave bottom boundary layer plays an important role in the suspension and transport of sediment (Beach and Sternberg, 1992) and in the estimation of bottom friction for mean currents (Grant and Madsen, 1979; Haines and Sallenger, 1994; Trowbridge and Agrawal, 1995). Because the flow reverses each half wave period and the introduction of turbulence is unsteady, traditional unidirectional flow boundary layer solution techniques are not valid.

Historically, turbulent wave bottom boundary layer models have been forced in the free stream with monochromatic waves and have approximated Reynolds stresses with time-invariant eddy viscosity models as is done in unidirectional steady turbulent boundary layers (Grant and Madsen, 1979; Smith, 1977). Trowbridge and Madsen (1984, herein TM84) included the second harmonic along with the fundamental frequency in the free stream forcing and a time- and depth-dependent eddy viscosity model. A semi-analytic solution for an oscillatory boundary layer due to monochromatic tidal fluctuations considering a time- and depth-dependent separable eddy viscosity model is presented by Lavelle and Mojfeld (1983). In Lavelle and Mojfeld, a solvable boundary value problem results from transforming a monochromatic cross-shore velocity to a time-distorted coordinate system, whereas the solution technique presented here transforms the cross-shore velocity to a distorted spatial domain. Each of these models yield reasonable comparisons with monochromatic laboratory data. However, extensions to the coastal zone require a solution for a spectrum of skewed and asymmetric waves which produces an unsteady introduction of turbulence.

One of the first wave bottom boundary layer models to consider a spectrum of waves is that of Beach and Sternberg (1992, herein, BS92). Over each half wave period, specified by consecutive zero-crossings, the eddy viscosity is assumed time-invariant and depth-dependent. Consecutive 256 second blocks of the free stream velocity are decomposed into spectral components. Smith (1977, herein S77) monochromatic time-invariant eddy viscosity model is forced with each spectral component over each half-wave period and linear superposition is used to reconstruct the complete solution. Similar spectral decomposition's have been performed by Madsen and Wikramanayake (1991). These models succeed in estimating the vertical structure of horizontal velocity under random waves, however, nonlinearities due to turbulent mixing as well as variations in turbulent mixing within a wave cycle are neglected.

One- and two-equation fully numerical turbulent kinetic energy models for monochromatic waves are reviewed in Fredsoe and Diegaard (1992). These models highlight the need for time- and depth-dependent turbulent mixing parameterization. Al-Salem (1993) compared the friction factor for numerical mixing length models and one equation and two equation models and found only minimal differences, implying that simple mixing length models are relatively robust. While the one- and two-equation models show much promise, they are currently used only in modelling simple monochromatic waves.

This work has been motivated by the desire to perform time-domain comparisons of field observations of velocity and/or bed stress with a model governed by the simple, order 1, physics of the wave bottom boundary layer. This paper presents a time-domain analytic solution to the linearized governing equation of the wave bottom boundary layer dynamics under random wave forcing assuming a separable time- and depth-dependent eddy viscosity. Section 2 presents the linearized equations governing the fluid dynamics in this near bed region. In Section 3, the time-dependent upper boundary condition is mapped through the domain, creating a new, well-posed, solvable, initial, boundary value problem. The separation of variables technique is applied, resulting in an analytic solution for the vertical and temporal structure of the wave bottom boundary layer cross-shore velocity. The time-dependent component of the eddy viscosity is formulated in Section 4. The results and discussion are presented in Section 5 and the conclusions are given in Section 6.

2. Governing equation

The linearized one dimensional time-dependent governing equation for the wave bottom boundary layer is (TM84; S77):

$$\frac{\partial \hat{u}}{\partial t} - \frac{\partial u_\infty}{\partial t} = \frac{1}{\rho}\frac{\partial \tau_{zx}}{\partial z} \tag{1}$$

where $\hat{u}$ is the cross-shore velocity within the domain, u_∞u is the free stream cross-shore velocity at the top of the domain, t is time, and z is the vertical coordinate (positive upward from the bed). This equation assumes that the pressure gradient may be approximated with the local acceleration. Guza and Thornton (1980) showed that although there exists a non-linear evolution of surface waves in the nearshore region, the local non-linearity is not extremely strong and the local wave field may be viewed as the superposition of phase-coupled free waves. For this investigation, this assumption is extended through the boundary layer and the local effect of the non-linear acceleration term is neglected. Furthermore, this model is not valid on plunging breaker beaches where the vertical momentum due to breaking waves may not be neglected. The turbulent stress, τ_{zx}, is represented with an eddy viscosity model with

$$\tau_{zx} = \rho\nu_t \frac{\partial \hat{u}}{\partial z}\,, \tag{2}$$

where ν_t is the eddy viscosity. The boundary and initial conditions are defined as

$$\hat{u}(d,t) = u_\infty, \tag{3a}$$

$$\hat{u}(z_o,t) = 0, \tag{3b}$$

and

$$\hat{u}(z,t_o) = \hat{r}(z), \tag{3c}$$

where d is the upper bound of the domain and is greater than δ, the boundary layer thickness, z_o is the bed roughness, t_o is the initial time, and $\hat{r}$ is the initial condition. A sketch of the boundary layer structure is shown in Fig. 1. The bed roughness is assumed to be known and time-independent. An alternative free stream boundary condition of $\partial\hat{u}(d,t)/\partial z = 0$ may also be used; the derivation is presented in Appendix A and is analogous to the one used here. Because of the second order nature of the boundary condition in the second formulation, transients take longer to decay and therefore the formulation presented below is recommended. For the conditions of

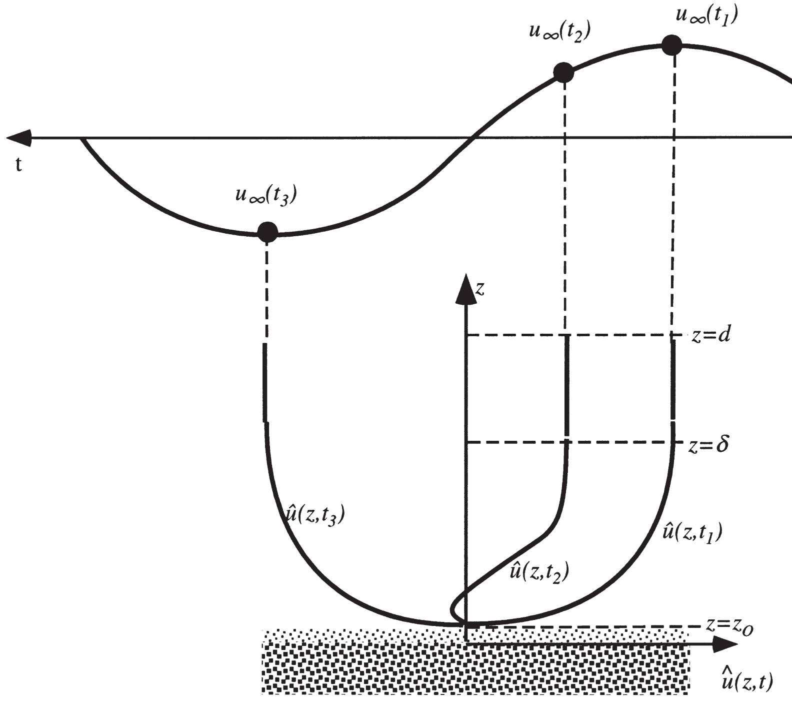

Fig. 1. Sketch of the boundary layer structure.

this solution technique to be met, the turbulent mixing coefficient, or eddy viscosity, must depend on independent characteristic length and time scales, and is modelled as

$$\nu_t = p(z)g(t), \tag{4}$$

where $p(z)$ and $g(t)$ contain the vertical and temporal component of the eddy viscosity, respectively. As is historically done, we consider the specific case when the eddy viscosity is defined as the product of a temporally varying velocity scale and linearly varying length scale,

$$\nu_t = \kappa u_* z, \tag{5}$$

such that $p(z) = z$ and $g(t) = \kappa u_*(t)$ and where κ is the Von Karman's constant and $u_*(t)$ is the time-dependent shear velocity at the bed ($z = z_o$). The eddy viscosity model assumes that the generation of turbulence in the boundary layer occurs at the bed, and scales with the distance from the bed. We note that the solution technique presented here is not restricted to this particular selection of eddy viscosity model and that any separable model for the eddy viscosity may be used. The substitution for p and g will not be made until needed.

3. Solution

The time-dependent random nature of the free stream velocity at the upper boundary condition limits the available mathematical solution techniques. To circumvent this limitation, we map the upper time-dependent boundary condition through the domain, transforming the governing equation to eliminate the time-dependency of the upper boundary condition. The transformation is defined with

$$u = \hat{u} - \frac{z - z_o}{d - z_o} u_\infty, \tag{6}$$

where u is the transformed cross-shore boundary layer velocity. Inserting (6) into (1), the governing equation and boundary and initial conditions become

$$\frac{\partial u}{\partial t} - \frac{d - z}{d - z_o}\frac{\partial u_\infty}{\partial t} = \frac{\partial}{\partial z}\left(\nu_t \frac{\partial u}{\partial z}\right) + \frac{\partial \nu_t}{\partial z}\frac{u_\infty}{d - z_o}, \tag{7a}$$

with boundary and initial conditions

$$u(d,t) = 0 \tag{7b}$$

$$u(z_o,t) = 0, \tag{7c}$$

and

$$u(z,t_o) = r(z) = (\hat{r})(z) - \frac{z - z_o}{d - z_o} u_\infty(t_o), \tag{7d}$$

where $r(z)$ is the transformed initial condition. The added forcing terms in (7a) result from mapping the upper boundary condition through the domain. This new governing equation is separable. Fig. 2 shows an illustration of the transformed velocity.

To solve (7), the homogeneous terms are moved to the left-hand side and forcing terms to the right,

$$\frac{\partial u}{\partial t} - g\,\frac{dp}{dz}\,\frac{\partial u}{\partial z} - pg\,\frac{\partial^2 u}{\partial z^2} = \frac{d-z}{d-z_o}\,\frac{\partial u_\infty}{\partial t} + g\,\frac{dp}{dz}\,\frac{u_\infty}{d-z_o}\,. \tag{8}$$

First we solve the homogeneous equation

$$\frac{\partial u_p}{\partial t} - g\,\frac{dp}{dz}\,\frac{\partial u_p}{\partial z} - pg\,\frac{\partial^2 u_p}{\partial z^2} = 0, \tag{9a}$$

with boundary and initial conditions

$$u_p(d,t) = 0, \tag{9b}$$

$$u_p(z_o,t) = 0, \tag{9c}$$

and

$$u_p(z,t_o) = r(z), \tag{9d}$$

where u_p, is the particular solution to the homogeneous equation and is solved with the separation of variables technique, such that $u_p \equiv \Psi(z)T(t)$. Substitution of this definition into (9a) results in

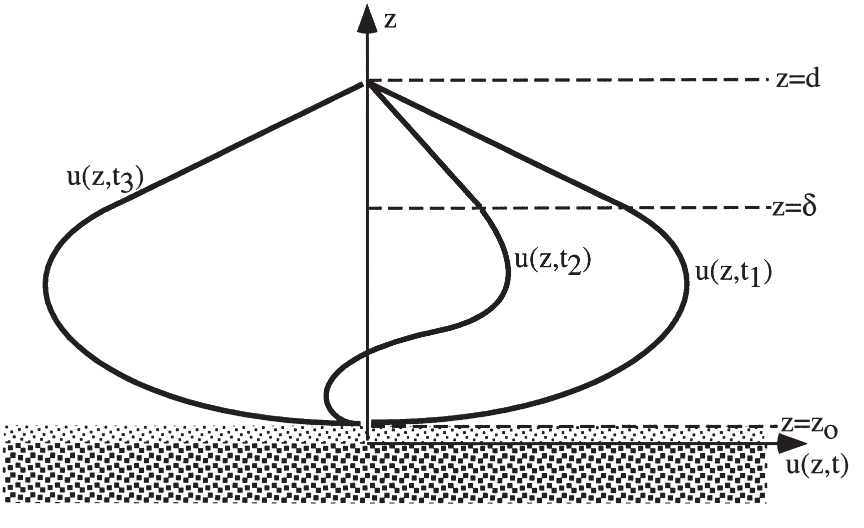

Fig. 2. Sketch of the transformed boundary layer structure.

$$\frac{\dot{T}}{gT} = \frac{p\Psi'' + p'\Psi'}{\Psi} = -\lambda^2 \tag{10}$$

where $(\cdot)$ is the derivative with respect to time, $(')$ is the derivative with respect to z and λ is the separation constant. (10) is represented by two ordinary differential equations

$$\dot{T} + \lambda^2 gT = 0, \tag{11a}$$

and

$$p\Psi'' + p'\Psi' + \lambda^2\Psi = 0. \tag{11b}$$

The unique solution for (11a) is

$$T(t) = A\exp^{(-\lambda^2\int_0^t g(\tau)\,\mathrm{d}\tau)}, \tag{12}$$

where A is an integration constant.$\Psi(z)$ is determined by substituting for p with the previous assumption, $p(z) = z$, into (11), leading to

$$z\Psi'' + \Psi' + \lambda^2\Psi = 0, \tag{13a}$$

with boundary conditions

$$\Psi(z_o) = 0 \tag{13b}$$

$$\Psi(d) = 0. \tag{13c}$$

If the vertical structure of the eddy viscosity, $p(z)$, is arbitrary, a numerical solution may be required for Ψ but is attainable. The solution for the vertically linear eddy viscosity problem is given by zeroth order Bessel functions of the first (J_o) and second kinds (Y_o)

$$\Psi = B_1J_o(2\lambda z^{\frac{1}{2}}) + B_2Y_o(2\lambda z^{\frac{1}{2}}), \tag{14}$$

where B_1 and B_2 are integration constants and are determined from the lower boundary condition. The upper boundary condition requires that the eigenvalues, λ_n, satisfy

$$J_o(2\lambda_n z_o^{\frac{1}{2}})Y_o(2\lambda_n d^{\frac{1}{2}}) - Y_o(2\lambda_n z_o^{\frac{1}{2}})J_o(2\lambda_n d^{\frac{1}{2}}) = 0. \tag{15}$$

The complete homogeneous solution becomes

$$u_p(z,t) = \sum_{n=1}^{\infty} b_n(J_o(2\lambda_n z_o^{\frac{1}{2}})Y_o(2\lambda_n z^{\frac{1}{2}}) - Y_o(2\lambda_n z_o^{\frac{1}{2}})J_o(2\lambda_n z^{\frac{1}{2}}))\exp^{(-\lambda_n^2\int_0^t g(\tau)\,\mathrm{d}\tau)} \tag{16}$$

where the new integration constants, b_n, are

$$b_n = \frac{1}{c_n}\int_{z_o}^{d} r(z)\Psi(z)\,\mathrm{d}z, \tag{17}$$

and the constant c_n satisfies the orthogonality condition below

$$\int_{z_o}^{d} \Psi_n(z)\Psi_m(z)\,\mathrm{d}z = \begin{cases} 0 & \text{if } m \neq n, \\ c_n & \text{if } m = n. \end{cases} \tag{18}$$

After the particular solution (16) is solved from the homogeneous equations, the non-homogeneous equation are determined. Rearranging (7) to

$$\frac{\partial u}{\partial t} = \frac{\partial}{\partial z}\left(\nu_t \frac{\partial u}{\partial z}\right) + F(z,t), \tag{19}$$

where the forcing term, $F(z,t)$ is the right-hand side of (8) and is a function of the free stream acceleration and velocity

$$F(z,t) \equiv \frac{d-z}{d-z_o}\frac{du_\infty}{dt} + g(t)\,\frac{u_\infty}{d-z_o}\,. \tag{20}$$

(19) is solved by assuming a series solution for the velocity of the form

$$u(z,t) = \sum_{n=1}^{\infty} a_n(t)\Psi_n(z), \tag{21}$$

where the eigenfunction, $\Psi_n(z)$, is known from (14), and $a_n(t)$ are the amplitude functions which are determined by substituting (21) into (19)

$$\sum_{n=1}^{\infty} \dot{a}_n\Psi_n = g\sum_{n=1}^{\infty} a_n(p\Psi_n{}')' + F. \tag{22}$$

Furthermore, assume F may also be represented with a series solution as

$$F(z,t) = \sum_{n=1}^{\infty} F_n(t)\Psi_n(z), \tag{23}$$

and F_n is determined with

$$F_n(t) = \frac{1}{c_n}\int_{z_o}^{d} F(z,t)\Psi(z)\,\mathrm{d}z. \tag{24}$$

Because $\Psi(z_o) = 0$ and $\Psi(d) = 0$, this definition for F will result in discontinuities at $z = z_o$ and $z = d$. Providing that the spatial step is small, and an adequate number of modes are considered, the effects of this discontinuity will be minimal. After substituting (23) into (22) and eliminating Ψ_n, (22) simplifies to

$$\dot{a}_n(t) + \lambda_n^2 g(t) a_n(t) = F_n(t). \tag{25}$$

Multiply (25) by $\exp^{(\lambda_n^2 \int_0^t g(\tau)\, \mathrm{d}\tau)}$ and combine the left-hand side into one derivative with respect to time

$$\frac{\mathrm{d}}{\mathrm{d}t}(\exp^{(\lambda_n^2 \int_0^t g(\tau)\, \mathrm{d}\tau)} a_n(t)) = F_n(t) \exp^{(\lambda_n^2 \int_0^t g(\tau)\, \mathrm{d}\tau)}. \tag{26}$$

Integrate (26) with respect to time to obtain an expression for the amplitude function

$$a_n(t) = a_n(0) \exp^{(-\lambda_n^2 \int_0^t g(\tau)\, \mathrm{d}\tau)} + \int_0^t F_n(\sigma) \exp^{(\lambda_n^2 \int_\sigma^t g(\tau)\, \mathrm{d}\tau)}\, \mathrm{d}\sigma \tag{27}$$

where the initial condition, $a_n(0) = b_n$, given in (17). The first term in (27) is the transient component which depends on the initial condition and decays to zero after the initial time, t_0. The second term in (27) is a weighted sum of the forcing. The weights represent a time history of the mixing for each mode. The time history term decays with time lag and the decay rate increases with increasing bed shear velocity. The complete solution to (1) is

$$\hat{u}(z,t) = \sum_{n=1}^{\infty} a_n(t) \Psi_n(z) + \frac{z - z_o}{d - z_o} u_\infty, \tag{28}$$

where

$$\Psi = Y_o(2\lambda_n z_o^{\frac{1}{2}}) J_o(2\lambda_n z^{\frac{1}{2}}) - J_o(2\lambda_n z_o^{\frac{1}{2}}) Y_o(2\lambda_n z^{\frac{1}{2}}),$$

(28) is the complete solution to the governing equation for the bottom boundary layer under an arbitraryfree stream random wave field. Although the vertical dependence of the eddy viscosity, $p(z)$, has been specified as linear, no assumptions have been made about the free stream forcing or the time-dependent nature of the turbulent mixing. The time-dependent component of the eddy viscosity, $g(t)$, is formulated in the next section.

4. Shear velocity formulation

Recall from (5), the time-dependent component of the eddy viscosity is assumed to be $g = \kappa u_*(t)$. Here the bed shear velocity, u_*, is defined with the equation (Townsend, 1976)

$$u_*(t) = \kappa z_o \left| \frac{\partial u}{\partial z} \right|_{z = z_o}. \tag{29}$$

Initially, $\left|\frac{\partial u}{\partial z}\right|_{z=z_o}$ is unknown and u_* is initialized, following S77 and BS92, with a constant stress boundary layer,

$$\hat{u}(z,t) = \frac{u_*(t)}{\kappa}\ln\left(\frac{z}{z_o}\right). \tag{30}$$

By assuming the velocity outside the boundary layer and boundary layer thickness are known, the first estimate of the shear velocity at the bed is given by

$$u_*(t) = \frac{\kappa u_\infty(t)}{\ln\left(\frac{\delta(t)}{z_o}\right)}, \tag{31}$$

where δ is the boundary layer thickness. For the initial iteration, the boundary layer thickness and shear velocity at time t are assumed to be constant over each half wave period, as specified by zero crossings of the given free stream velocity (BS92) and the solution is determined by iterating on

$$\delta = \frac{u_{*_{\text{peak}}}}{2\omega} \tag{32a}$$

and

$$u_{*_{\text{peak}}} = \frac{\kappa u_{\text{peak}}(t)}{\ln\left(\frac{\delta}{z_o}\right)} \tag{32b}$$

where u_{peak} is the peak amplitude of the free stream velocity at each half wave zero crossing. After the first iteration of the complete solution, the velocity gradient at the bed is determined and, a new fully time-dependent u_* is calculated directly from

$$u_*(t) = \sum_{n=1}^{\infty} -\kappa\lambda_n z_o^{\frac{1}{2}} a_n(t)\left(Y_o(2\lambda_n z_o^{\frac{1}{2}})J_1(2\lambda_n z_o^{\frac{1}{2}}) - J_o(2\lambda_n z_o^{\frac{1}{2}})Y_1(2\lambda_n z_o^{\frac{1}{2}})\right) + \frac{\kappa z_o u_\infty}{d - z_o}. \tag{33}$$

The complete solution is iterated until u_* converges.

Given the above selection for u_*, there exists the possibility of a mild singularity in (1) when $u_*(t) = 0$ (this occurs when the sign of $\left.\frac{\partial u}{\partial z}\right|_{z=z_o}$ changes direction). The manifestation of the singularity has not been present, because the solution is represented with a finite number of modes and because the definition of u_* is discrete in nature, therefore it is rarely identically zero.

5. Results and discussion

The solution for the time- and depth-dependent velocities in the wave boundary layer is given by (28). Unless otherwise specified, the investigations presented here will assume the following parameter specifications: (1) the lower boundary of the domain, given by the bottom roughness, z_o, is 0.1 cm and (2) the upper boundary is 20 cm (the choice of d is discussed later in this section). For numerical efficiency, both course and fine time steps are used. The course time step was chosen as 1/8 second to resolve the temporal structure of u_∞ and u_*. For each independent mode, a finer time step which resolves the integrand in (27) with 50 steps is determined, yielding an equivalent numerical accuracy for each mode. The initial condition is approximated with a logarithmic profile (30)

$$r(z) = \frac{u_{*_{\text{peak}}} = (t_o)}{\kappa} \ln\left(\frac{z}{z_o}\right). \tag{34}$$

For increased resolution in the near bed region, the vertical spatial grid is defined with a log transform. The spatial resolution must be large enough to resolve the highest considered modal structure.

Fig. 3 shows the vertical structure of the eigenfunctions and the temporal variations of amplitude for the first 4 modes of a 5 s monochromatic wave with a 100 cm/s amplitude, a typical ocean wave often observed in nature. The relative amplitude of the higher modes increases during the period of flow reversal, when the boundary layer structure deviates from the simple logarithmic structure. Higher modes continue to be included until the rms of the amplitude function for a particular mode is less than 0.1% of the summed rms of the previous modes (Fig. 4(a)). The velocity solution is assumed to have converged when the rms deviation in maximum shear velocity between consecutive iterations is less than 1% of the rms of the previous iteration, this generally occurs in less than 8 iterations (Fig. 4(b)).

The model's sensitivity to the upper boundary elevation, d, is examined with the rms deviation of the model solution between a domain size of 50 cm and domain sizes of 10, 20, 30, and 40 cm (Fig. 5). As shown in the figure, the normalized rms deviation between domain sizes of 20 and 50 cm has a maximum of 3.5% at the bed. For this investigation, we assume that a domain size of 20 cm is adequate. The authors recognize that more sophisticated selections of the vertical structure of the eddy viscosity, p, such as an exponentially decaying model, may decrease the sensitivity of the model to the selection of the upper domain. However, we have elected to include the simpler linear model, $p = z$, which does not introduce any additional tuning parameters. For comparison of the model with data, we use the free stream elevation, as specified by the observations.

The model qualitatively reproduces the laboratory observations of Jonsson and Carlsen (1976; Fig. 6). The upper boundary, d, was specified to be the free stream elevation of 17 cm and the lower boundary, z_o, was specified to be the measured bottom roughness of 0.077 cm. The rms of the deviation between the model and data over both the wave phase and elevation is shown in Fig. 7. The rms deviation

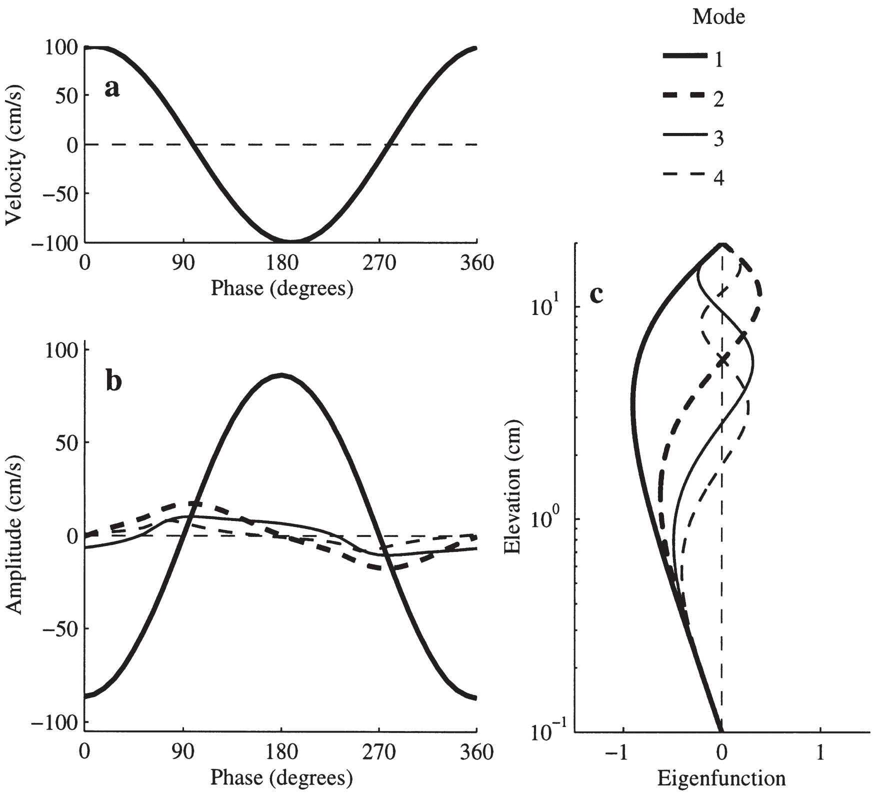

Fig. 3. Temporal and spatial structure of predicted cross shore velocity for the first four modes: (a) input free stream velocity, u_∞; (b) temporal amplitude, $a_n(t)$; (c) spatial eigenfunction, $\Psi_n(z)$; $T = 5$ s, $u_o = 100$ cm/s, $z_o = 0.1$ cm, $d = 10$ cm, number of spatial steps = 400.

of the velocity calculated over the elevation at each phase shows the largest deviation occurs preceding the peak velocity at phases between 120° and 150° and between 300° and 330°. The rms deviation calculated over the wave phase at each elevation shows the best correlation at both the upper and lower boundaries and the largest deviation in the velocity overshoot region. The model's discrepancy with the data within the overshoot region may possibly be attributed to either the linear vertical structure of the eddy viscosity model or unaccounted tank circulation. BS92 have increased model agreement in this region by assuming an exponentially capped eddy viscosity model. The model's prediction of the bed shear velocity, u_*, is in good agreement (correlation coefficient is 0.95) with measurements (Fig. 8).

Similarly, the model is compared with the more recent laboratory observations of Jensen et al. (1989). The rms of the deviation between the model and data over both the wave phase and elevation is shown in Fig. 9. The upper boundary, d, was specified to be the free stream elevation of 17 cm and the lower boundary, z_o, was specified to be the measured bottom roughness of 0.003 cm. The rms deviations calculated

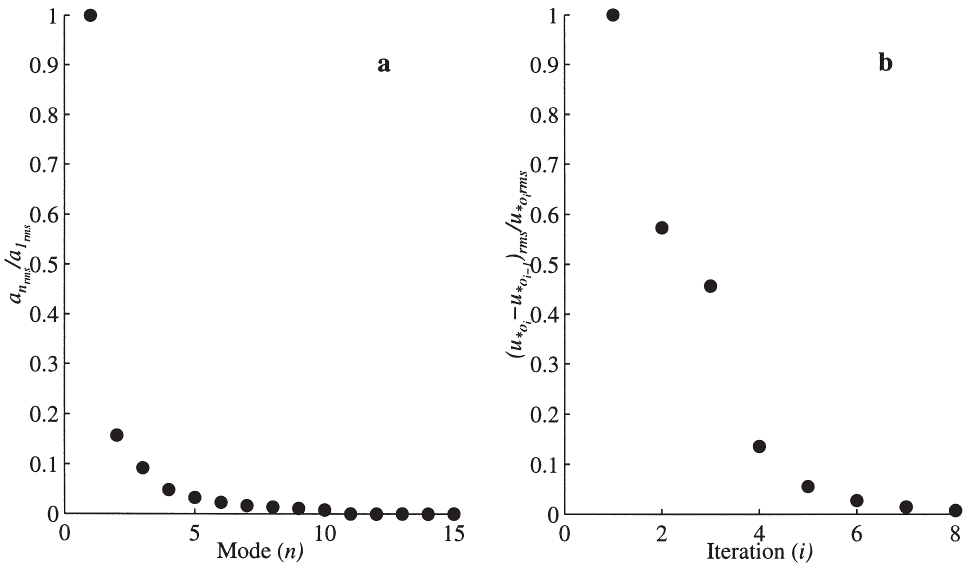

Fig. 4. (a) Series convergence is assumed when the rms of a given mode amplitude ($a_{n_{rms}}$) is $<$ 1% of the summed rms of the previous mode amplitude ($a_{1_{rms}}$), $a_{n_{rms}} \Sigma_{m=1}^{n-1} a_{m_{rms}} < 1\%$. (b) Solution convergence is assumed when the rms deviation of the bed shear velocity between two consecutive iterations $((u_{*_i} - u_{*_{i-1}})_{rms})$ is $<$ 1% of the rms of the first iteration ($u_{*i_{rms}}$), $(u_{*_i} - u_{*_{i-1}})_{rms}/(u_{*_i})_{rms} < 1\%$.

over the elevation at each wave phase are smaller than the deviations of the between the model and the Jonsson and Carlson observations. Future investigations could include tuning the vertical structure of the eddy viscosity model for better agreement to both sets of laboratory data.

The model was used to investigate the wave bottom boundary layer response to a variety of wave conditions similar to those observed in nature. To accomplish this, the wave bottom boundary layer response to a variety of input free stream wave conditions is quantified by evaluating the temporal distribution of bed shear velocities and by evaluating the spatial and frequency structure of the velocity variance. In the first investigation, the effect of free stream velocity and acceleration variations on the wave bottom boundary layer (herein, WBBL) are examined with three separate monochromatic waves. In the second investigation, the response of the WBBL to free stream velocities which have non-sinusoidal shapes is characterized with 36 cases of free stream velocities which have uniform variance and a variety of skewness and asymmetry values.

In the first investigation, three input monochromatic free stream wave cases ($u(t) = u_o\cos(\omega t)$) were considered with free stream rms velocities and accelerations ranging from 35.4 cm/s to 70.7 cm/s and from 88.6 cm/s^2 to 44.3 cm/s^2, respectively (Table 1). The response of the WBBL to each of the cases is evaluated with the calculated bed shear velocity, u_*. The largest bed shear velocity occurs in case 1 when both the rms velocity and acceleration are largest. In (1) the free stream acceler-

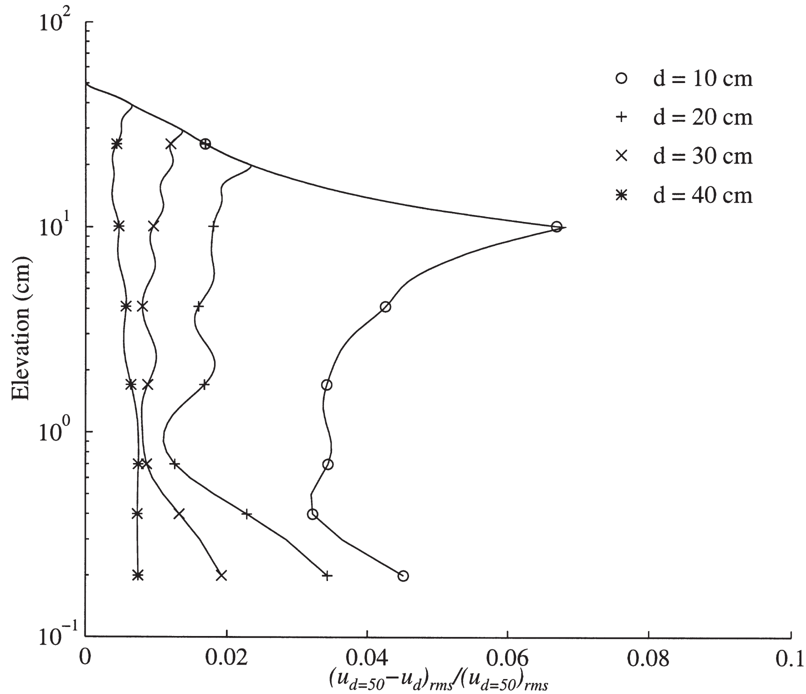

Fig. 5. The rms deviation between model results with a 50 cm upper boundary and model results with 10, 20, 30, and 40 upper boundaries normalized by the rms of the model results with a 50 cm upper boundary.

ation forces the WBBL dynamics, consequently a correlation between the bed shear and free stream acceleration is anticipated. The shear velocity also appears correlated to the free stream velocity. This is indicated by cases 2 and 3 where the free stream acceleration is held constant and the bed shear increases with increasing free stream velocity. In all cases, the shear velocity leads the free stream velocity by approximately 30°.

Comparing the model's predicted bed shear velocities with those predicted by (36a) and (36b) (a common method for scaling the bed shear velocity), it is found that $(u_*)_{\mathrm{peak}}$ exceeds $(u_*)_{\mathrm{rms}}$ by 12% to 14% (Table 1). Also, the large temporal variations of shear velocity as seen in observations (Fig. 8) and predicted by this model are neglected by scaling the shear velocity as uniform over the wave phase, as in (32a) and (32b). For each monochromatic wave case, the power spectrum of the velocity at three elevations with in the boundary layer is presented in Fig. 10. As expected, the energy at the fundamental frequency decreases with decreasing elevation. As z approaches z_o, the weakly nonlinear interaction of the right-hand side of (1) between u_* and $\partial u/\partial z$ increases and results in transfer of energy from the fundamental to other frequencies. As a crude approximation for illustrative purposes,

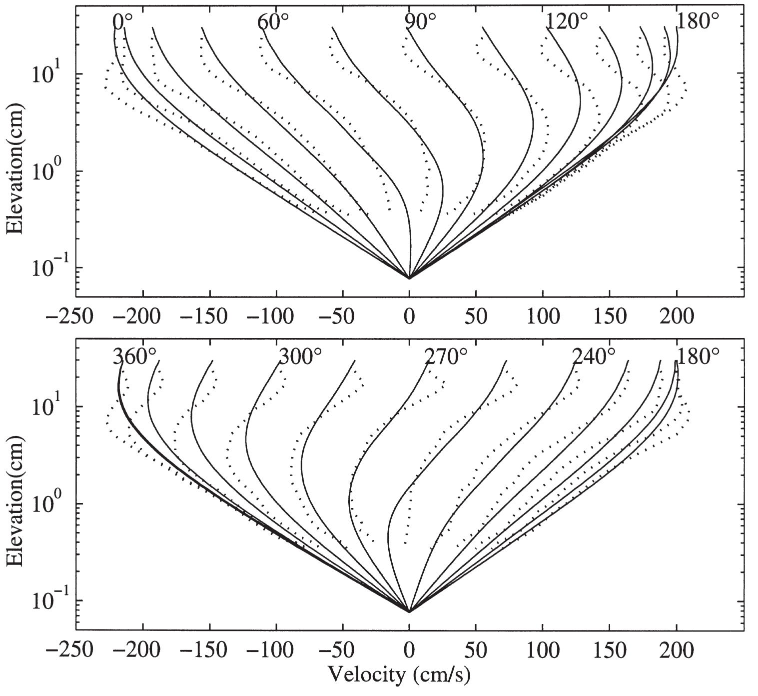

Fig. 6. Comparison between (—) model and (…) measured (Jonsson and Carlsen, 1976) cross shore velocities over the wave phase.

assume that $\left.\frac{\partial u}{\partial z}\right|_{z=z_o}$ varies as a sinusoidal wave, $\sin(\omega t)$. At the bed, the right-hand side of (1) varies with

$$\left.\frac{\partial \tau}{\partial z}\right|_{z=z_o} \propto |\sin(\omega t)|\sin(\omega t) \tag{35}$$

$$\frac{1}{\pi}\left(\frac{8}{3}\sin(\omega t)-\frac{8}{15}\sin(3\omega t)-\frac{8}{105}\sin(5\omega t)\right).$$

Hence, for a monochromatic input wave, we expect energy to be present at the odd harmonics. For a bichromatic input wave, energy would be transferred to both sum and difference frequencies of the two input primary frequencies. In Fig. 10, the 5 s wave (cases 1 and 2), energy is present at 0.6 and 1 Hz and similarly, for the 10 sec wave (case 3), energy is present at 0.3 and 0.5 Hz. This result is in agreement with TM84, who observed that to match the variance at odd harmonics seen in the Jonsson and Carlsen data set, a time-varying u_* must be considered.

The relative amplitude at each elevation between the third and fifth harmonics of

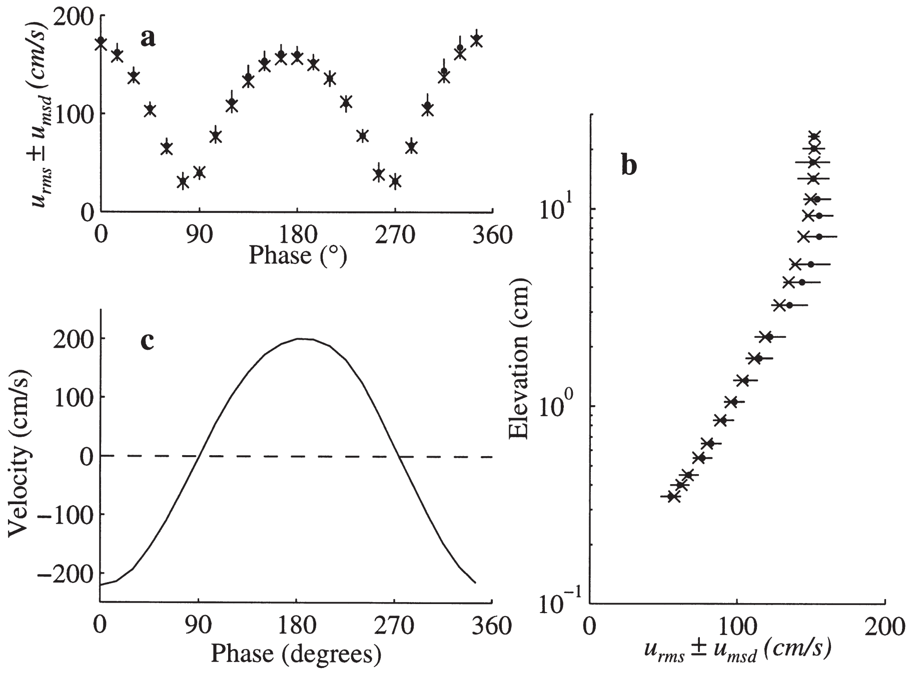

Fig. 7. Comparison of the rms velocity calculated (a) over the elevation at each wave phase, $u_{rms}(\theta) \pm u_{msd}(\theta)$; and (b) over the wave phase at each elevation, $u_{rms}(z) \pm u_{msd}(z)$; (×) model results and (·) measurements (Jonsson and Carlsen, 1976). Error bars indicate ± one root-mean-square-deviation (msd) between model results and measurements. (c) Input free stream velocity, u_∞.

velocity and the first harmonic of velocity show that these harmonics at the bed represent approximately 8 and 4% of the fundamental and decay as the elevation increases, (Fig. 11). Because of the phase shift in the WBBL, this weakly nonlinear interaction decreases with increasing elevation, as the phase shift between $\left|\frac{\partial u}{\partial z}\right|_{z=z_o}$ and $\partial u/\partial z$ increases.

The phase and amplitude of the cross-shore velocity vertical structure at the first (fundamental), third, and fifth harmonic frequencies is examined by calculating the cross spectral matrix between each elevation using the first mode of a frequency domain empirical orthogonal function (CEOF) (Wallace and Dickinson, 1972) (Fig. 12). In each case, the first mode describes at least 99% of the variance. As expected, the phase shift at the first harmonic increases with decreasing elevation and is approximately 30° at the bed. In contrast to the fundamental frequency, at both the third and fifth harmonic, the amplitude approaches zero at the upper domain, satisfying the upper boundary condition of a single frequency input velocity. Additionally, the phase associated with these harmonics is significantly larger than that of the fundamental frequency.

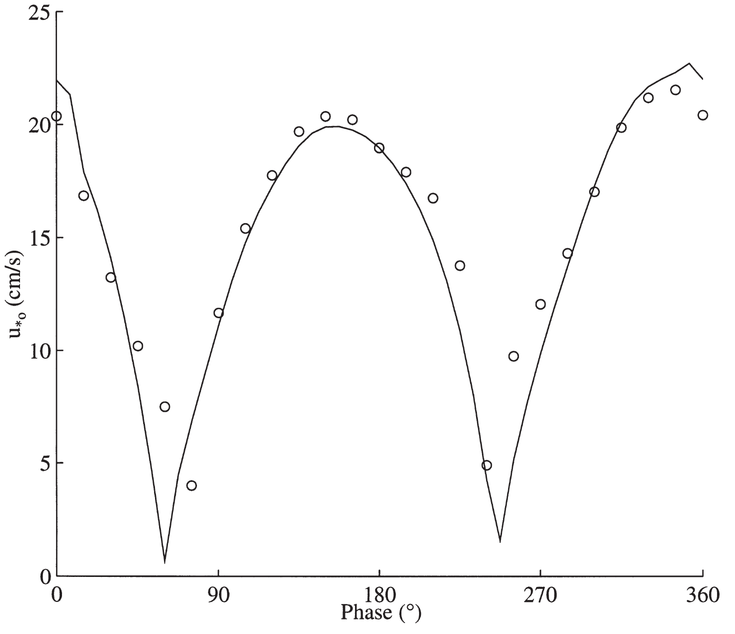

Fig. 8. The bed shear velocity, u_*, over the wave phase: (◦) measurements; and (—) model. The correlation coefficient between model results and measurements is 0.95.

In nature waves are never truly monochromatic and often have peaky (skewed) and sawtooth (asymmetric) shapes. Observations of shoaling surface gravity waves, indicate that both wave velocity skewness and asymmetry increase to their maximum values at the onset of breaking (Elgar et al., 1990). At the break point, the normalized wave skewness is as large as 0.6 and normalized wave asymmetry is as large as 1.2. The normalized third order moments are defined with the following equations (Elgar and Guza, 1985)

$$S = \frac{\langle u^3(t)\rangle}{\langle u^2(t)\rangle^{3/2}} \tag{36a}$$

$$A = \frac{\langle H(u)^3(t)\rangle}{\langle H(u)^2(t)\rangle^{3/2}} \tag{36b}$$

where $H(u)$ is the Hilbert transform of u.

The effect of free stream wave skewness and asymmetry on the response of the wave bottom boundary layer is investigated for 36 uniform variance input wave conditions with normalized skewness and asymmetry values varying from 0 to 0.625 and 0 to 1.25, respectively. The temporal distribution and amplitude of the predicted bed shear velocity of four of the extreme cases is shown to greatly vary with input skewness and asymmetry (Fig. 13). As in the monochromatic wave cases, the ratio

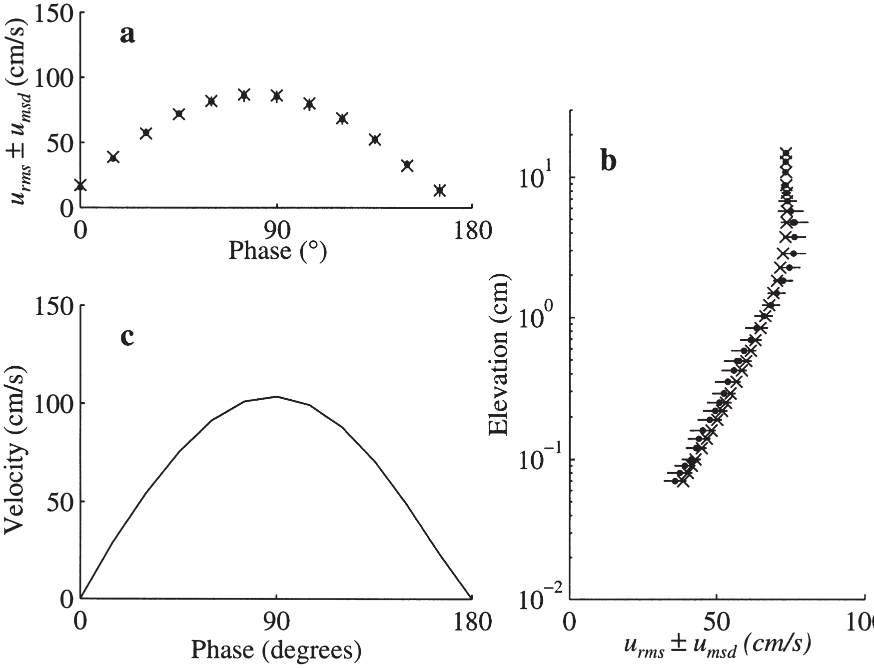

Fig. 9. Comparison of the rms velocity calculated (a) over the elevation at each wave phase, $u_{rms}(\theta) \pm u_{msd}(\theta)$; and (b) over the wave phase at each elevation, $u_{rms}(z) \pm u_{msd}(z)$; (*) model results and (·) measurements (Jensen et al., 1989). Error bars indicate ± 1msd between model results and measurements. (c) Input free stream velocity, u_∞.

Table 1
Predicted shear velocity for 3 monochromatic waves

Case	T (s)	u_0 (cm s^{-1})	$(u_\infty)_{\rm rms}$ (cm s^{-1})	$\left(\frac{du_\infty}{dt}\right)_{\rm rms}$ (cm s^{-2})	$(u_*)_{\rm peak}$ (cm s^{-1})	$(u_*)_{\rm max}$ (cm s^{-1})	$\langle(u_*)\rangle$ (cm s^{-1})
1	5	100	70.7	88.6	10.9	13.1	9.0
2	5	50	35.4	44.3	6.4	7.6	5.2
3	10	100	70.7	44.3	9.5	11.4	7.8

Bed shear velocity resulting from 3 independent monochromatic waves. Input wave period, T, and amplitude, u_o, conditions and rms free stream velocity, u_{rms}, and rms acceleration, du/dt_{rms}, for three independent wave cases. Also given is the characteristic boundary layer thickness and shear velocity as predicted by the Smith model and the rms, mean, and maximum bed shear velocity as predicted by the model presented in this paper.

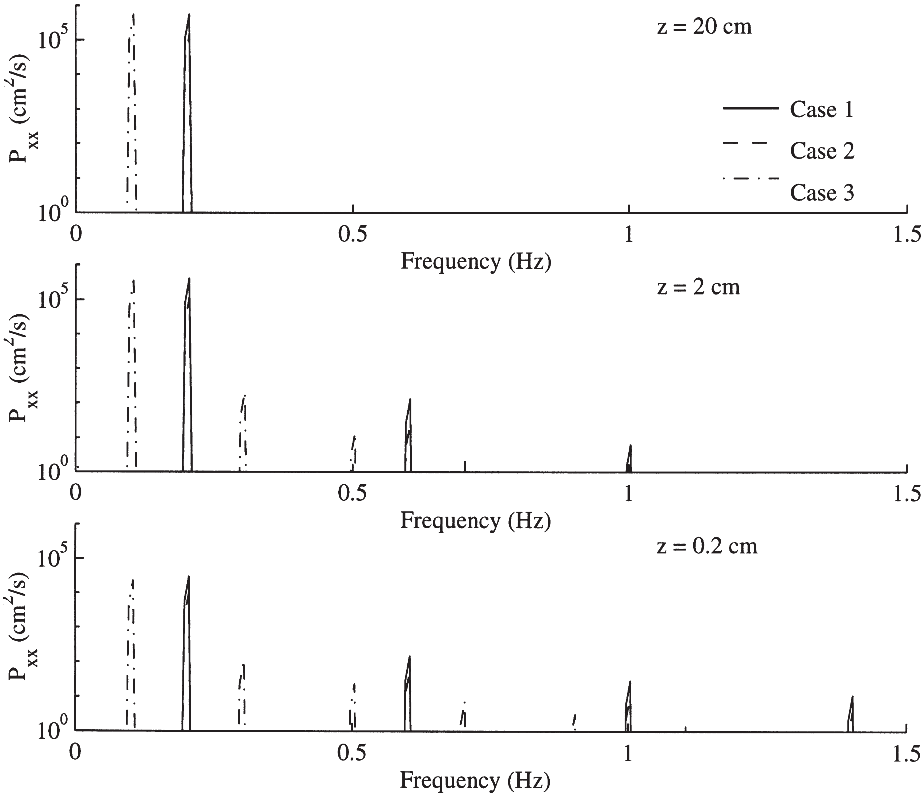

Fig. 10. Energy density spectra for each of the three cases at three elevations: Case 1, $T = 5$ s, $u_o = 100$ (cm/s); Case 2, $T = 5$ s, $u_o = 50$ (cm/s); Case 3, $T = 10$ s, $u_o = 100$ (cm/s).

of the third and fifth harmonics of the velocity to the first harmonic increases with decreasing elevation (Fig. 11). However, the third harmonic of velocity at the bed can be as large as 30% of the first harmonic of velocity when the combined effect of the maximum free stream velocity skewness and asymmetry, and the WBBL non-linearities are considered. Over the range of skewness and asymmetry values investigated, the harmonic amplitude ratio is shown to increase with increasing rms free stream wave acceleration which increases with increasing skewness and asymmetry (Fig. 14). The rms bed shear velocity, $(u_*)_{\mathrm{rms}}$, shows a mild increase with increasing skewness and asymmetry (Fig. 14).

Energetics-based basic sediment transport models assume the total sediment transport rate is proportional to the dimensionless velocity vector and the energy dissipation rate, or work done by the fluid on the bed, τ (Bowen, 1980 and Baillard, 1981). The transport due to suspended load, i_s, is proportional to

$$i_s \propto u_\infty |\tau_o u_\infty|. \tag{37}$$

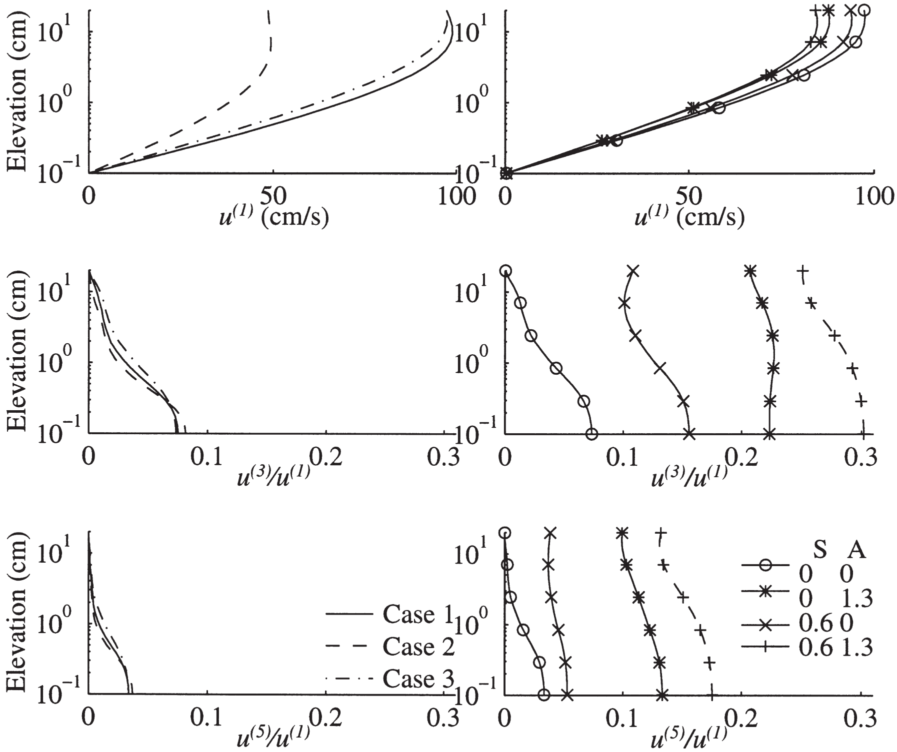

Fig. 11. The predicted amplitude of the first harmonic of velocity (top). The predicted relative amplitude of (middle) third and (bottom) fifth harmonics to the first harmonic. The left panels are the results for three monochromatic input waves and the right panels are the results for four skewed and asymmetric input waves. The superscripts $^{(1)}$, $^{(3)}$, and $^{(5)}$ denote the first, third and fifth harmonic, respectively.

Commonly, the bed stress is assumed to be a quadratic function of the velocity, $\tau_o = \rho f_w u_\infty^2$. Using a quadratic stress law, the time-averaged work done is large under skewed waves and zero under purely asymmetric waves. The model presented in this paper predicts the time-varying velocity and bed shear stress, allowing for the instantaneous computation of the energy dissipation rate without assuming a quadratic shear stress (Fig. 14). For comparison pruposes, we calculate the friction factor, f_w, with

$$f_w = \frac{\langle (u_*)^2 \rangle}{\langle u_\infty^2 \rangle}\,. \tag{38}$$

The sediment transport rate using both the quadratic stress law and this model is strongly dependent on the free stream wave skewness (Fig. 15). For a purely skewed wave (S = 0.6, A = 0), the transport rate predicted by this model will be 3 times larger than that predicted by a quadratic model. Furthermore the quadratic model

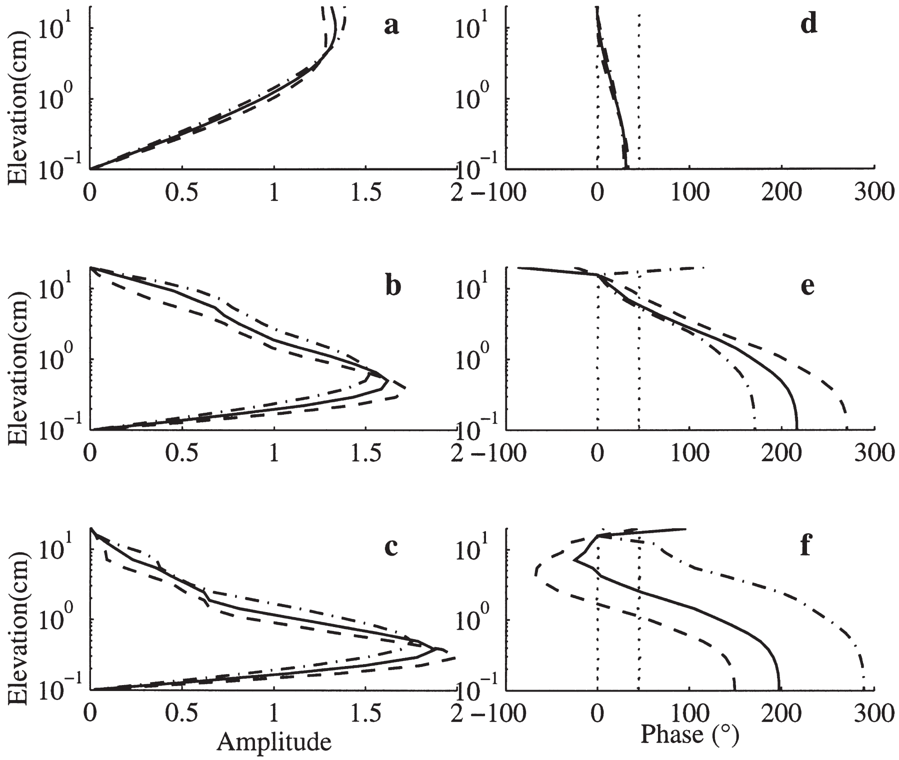

Fig. 12. Frequency domain EOF of the cross shore velocity at the (top) first, (middle) third, and (bottom) fifth harmonic: (a–c) amplitude (d–f) phase. Each line represents: (—) Case 1; (---) Case 2; (– • –) Case 3. In all cases, Mode 1 describes at least 99% of the variance.

predicts no dependency on wave asymmetry, but this model predicts the transport will decrease with decreasing asymmetry. Under a purely asymmetric wave (S = 0, A = 1.25), the transport will be negative, or offshore. This dependency is due to the phase shift between the free stream velocity and the shear stress. Fig. 15(d) shows the relative phase between the free stream velocity and the velocity immediately above the bed.

The model predicts a convergence of net suspended load transport at the break point where the skewness is maximum just prior to wave breaking and where the asymmetry is a maximum just after the waves are broken. This result is consistent with sediment models which predict the formation of sand bars at the breakpoint.

6. Conclusions

An analytic solution for the vertical and temporal structure of the wave bottom boundary layer, cross-shore velocity under arbitrary free stream wave forcing is

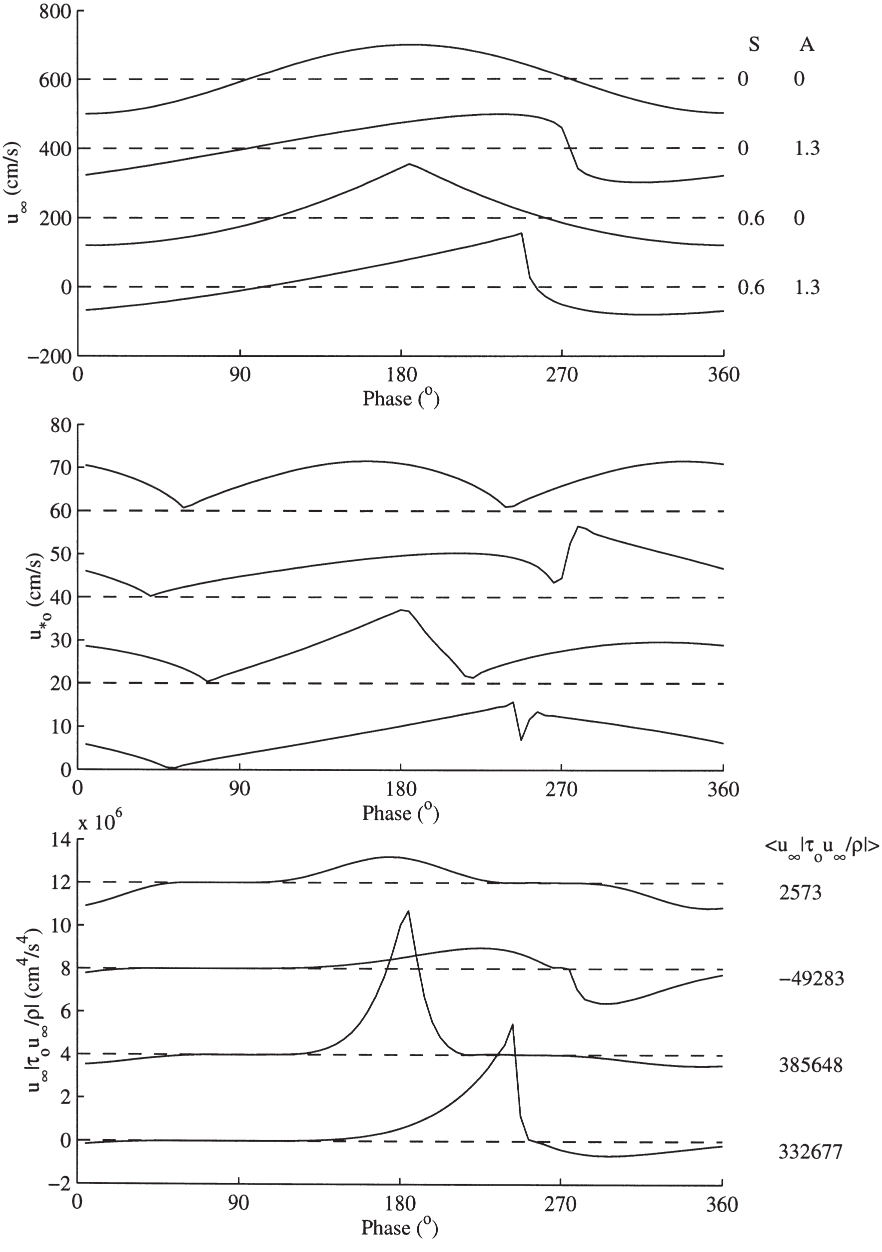

Fig. 13. Four separate input wave velocities (top) and the model predicted bed shear velocity (middle). The velocity times the work done on the bed, $u_\infty|\tau_o|u_\infty$, is given in the bottom panel and the mean value is given on the right hand side of the plot. All input waves have equal variance and different skewness and asymmetry values. Note that the curves in each of the three panels are offset by 200 cm/s, 20 cm/s, and 4×10^4 cm^4/s^4 (top to bottom).

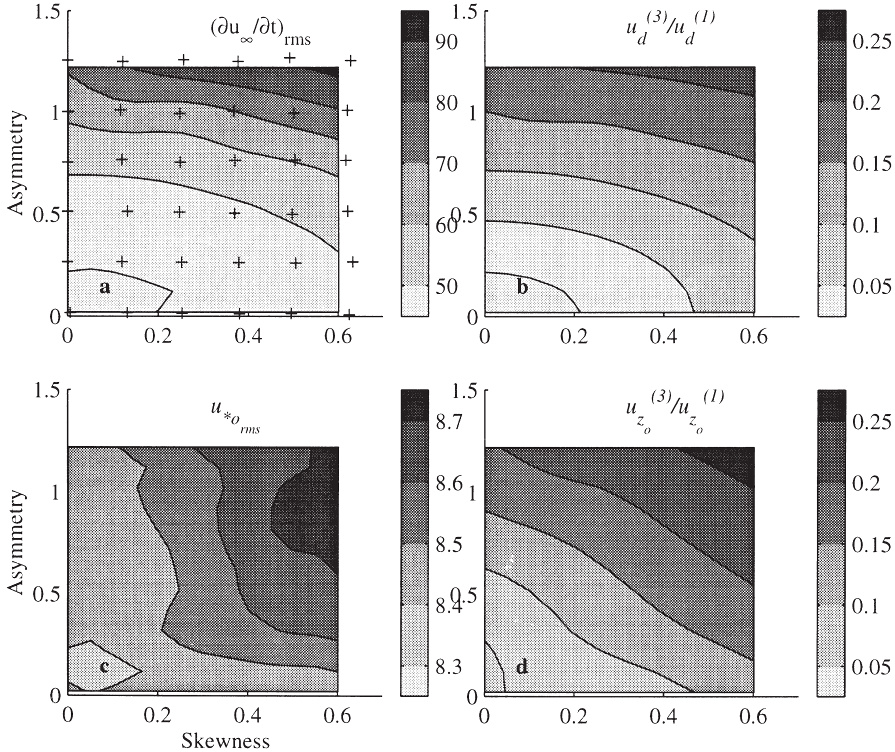

Fig. 14. Distribution of (a) rms free stream acceleration, $(\partial u_\infty/\partial t)_{rms}$; (b) predicted relative free stream velocity of the third harmonic to the first harmonic $u_d^{(3)}/u_d^{(1)}$; (c) rms bed shear velocity, $u_{*_{rms}}$; (d) predicted relative free stream velocity of the third harmonic to the first harmonic $u_{z_o}^{(3)}/u_{z_o}^{(1)}$ over free stream velocity skewness and asymmetry values ranging from 0 to 0.6 and 0 to 1.2, respectively. The 36 individual runs are indicated with + symbols.

derived. The eddy viscosity is represented as a separable functions of time- and depth. The time-dependent boundary condition $u(d,t) = u_\infty(t)$ is distributed through the solution domain with a transformation of $u(z,t)$ to create a well posed solvable initial boundary value problem with time-independent boundary conditions. The transformed equation is solved with the separation of variables technique. An analytic expression for the time- and depth-dependent cross-shore velocity is determined. No assumption has been made about the form of the input wave velocity, so the model is able to predict the temporal and vertical cross-shore velocity structure and the temporally varying bed shear for a random wave field.

Good agreement is found between the model predicted velocity structure and bed shear velocity and laboratory measurements. The correlation between the model predicted and measured bed shear velocity is 0.95. Predictions of the bed shear velocity under three independent monochromatic input wave velocities indicate that bed shear velocity increases with increasing wave velocity and acceleration

A weakly nonlinear interaction results from scaling the shear velocity with the

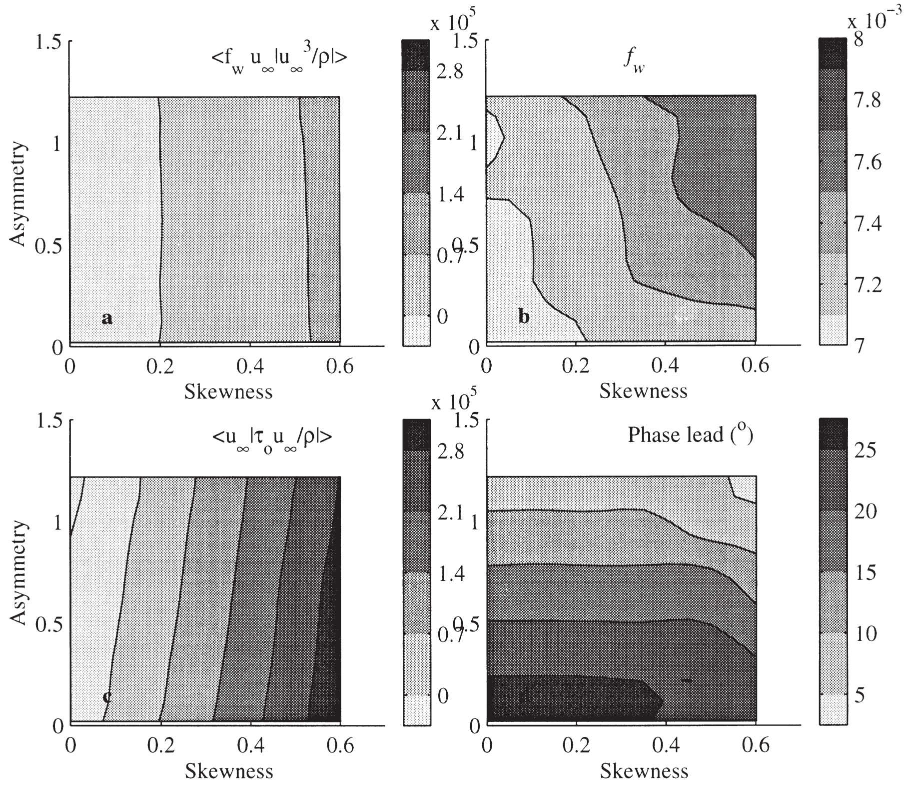

Fig. 15. Distribution of (a) the proportional sediment transport as computed with a quadratic stress law; (b) the friction factor, f_w; (c) the proportional sediment transport as computed with the model presented here; (d) the average phase lead of the u_{z_o} relative to the free stream velocity; over free stream velocity skewness and asymmetry values ranging from 0 to 0.6 and 0 to 1.2. respectively.

time-dependent velocity shear at the bed. The magnitude of the nonlinear interaction becomes larger as z approaches z_o, and at the bed, the shear stress, τ is proportional to

$$\tau \propto \left[\left| \frac{\partial u}{\partial z} \right| \frac{\partial u}{\partial z} \right]_{z = z_o}. \tag{39}$$

For a monochromatic free stream velocity, this interaction distributes input energy to odd harmonics. For the cases considered in this paper, the amplitude of the velocity energy density at the bed in the third harmonic is only 8% of the amplitude at the first harmonic. However, the combined effect of skewed and asymmetric input waves characteristic of those found in the coastal region and the nonlinear interactions results in amplitude ratios of as much as 30%. For monochromatic input wave velocities the effect of nonlinearities may be neglected, but for non-sinusoidal input wave velocities, as often found in nature, the energy in the higher harmonics may well have a significant effect.

The model also predicts the time-dependent structure of the bed shear velocity, which is shown to vary significantly over a wave period. The bed shear velocity is examined over a variety of skewed and asymmetric input wave forcing conditions. The rms bed shear velocity is slightly inscreased with increasing input wave skewness and asymmetry (which also indicates increased wave acceleration). However, the maximum bed shear velocity is shown to increase with increasing wave skewness and decreasing wave asymmetry, i.e. maximum bed shear occurs under the peakiest input waves.

In agreement with energetics based sediment transport models, the suspended sediment transport rate is shown to be strongly correlated to wave skewness and reach a maximum value under maximum free stream velocity skewness. Under purely asymmetric waves, the quantity is significantly smaller but is directed in the offshore direction. In contrast, simple quadratic stress models neglect phase and amplitude variations between velocity and shear stress and predict zero work done under asymmetric waves.

Acknowledgements

Funding for this work was provided for D. Foster by a Department of Defense ASEE fellowship and the Office of Naval Research, coastal dynamics program (grant N00014-9610237); for R. Holman by the Office of Naval Research, coastal dynamics program (grant N00014-9610237); and for R. Guenther by the Office of Naval Research, ocean engineering (grant 9610696). The first author wishes to acknowledge the time and helpful discussions with E. Thornton and M. Freilich. Early generations of this manuscript greatly benefit from edits by T. Lippmann, N. Plant, and H. Stockdon.

Appendix

The second formulation bounds the solution with a zero vertical gradient at some elevation outside the boundary layer. The boundary and initial conditions are defined to be

$$\hat{u}_2(d,t) = u_\infty, \tag{40a}$$

$$\hat{u}_2(z_o,t) = 0, \tag{40b}$$

and

$$\hat{u}_2(z,t_o) = \hat{r}(z), \tag{40c}$$

where d is a given elevation outside the boundary layer, z_o is the bed roughness, t_o is the initial time, and $\hat{r}$ is the initial condition. The same separable eddy viscosity model as given in (4) is used. In this formulation, a variable transformation is not necessary as the boundary conditions are time independent. As before, separate the homogeneous and non-homogeneous terms of (1),

$$\frac{\partial u_2}{\partial t} - g\,\frac{\mathrm{d}p}{\mathrm{d}z}\,\frac{\partial u_2}{\partial z} - pg\,\frac{\partial^2 u_2}{\partial z^2} = \frac{\partial u_\infty}{\partial t}\ . \tag{41}$$

where u_2 is the complete solution for formulation two. The non-homogeneous term, simpler than in formulation one, is independent of z and the homogeneous equation is identical to (9a)

$$\frac{\partial u_p}{\partial t} - g\,\frac{\mathrm{d}p}{\mathrm{d}z}\,\frac{\partial u_p}{\partial z} - pg\,\frac{\partial^2 u_p}{\partial z^2} = 0, \tag{42a}$$

with boundary and initial conditions

$$\frac{\partial u_{2_p}}{\partial z}\,(d,t) = 0, \tag{42b}$$

$$u_{2_p}(z_o,t) = 0, \tag{42c}$$

and

$$u_{2_p}(z,t_o) = r(z), \tag{42d}$$

Solution-Formulation Two

As in the previous derivation, solve for the particular solution, $u_{p_2} = Y(z)T(t)$ with the separation of variables technique. In this formulation, the determination of the eigenvalue, l, is determined by searching a combination of zero and first order Bessel functions for zero crossings,

$$J_o(2\lambda_n z_o^{\frac{1}{2}})Y_1(2\lambda_n d^{\frac{1}{2}}) - Y_o(2\lambda_n z_o^{\frac{1}{2}})J_1(2\lambda_n d^{\frac{1}{2}}) = 0. \tag{43}$$

The complete homogeneous solution becomes

$$u_{2_p}(z,t) = \sum_{n=1}^{\infty} b_{2_n}(J_o(2\lambda_n z_o^{\frac{1}{2}})Y_o(2\lambda_n z^{\frac{1}{2}}) - Y_o(2\lambda_n z_o^{\frac{1}{2}})J_o(2\lambda_n z^{\frac{1}{2}})\exp^{(-\lambda_n^2\int_0^t g(\tau)\,\mathrm{d}\tau)} \tag{44}$$

where the integration constant and orthogonality condition have the same form as (17) and (18), respectively,

$$b_n = \frac{1}{c_n}\int_{z_o}^{d} r(z)\Psi(z)\,\mathrm{d}z,$$

and below

$$\int_{z_o}^{d} \Psi_n(z)\Psi_m(z)\,\mathrm{d}z = \begin{cases} 0 & \text{if} \quad m \neq n, \\ c_n & \text{if} \quad m = n. \end{cases}$$

The non homogeneous component of the solution given by

$$\frac{\partial u_2}{\partial t} = \frac{\partial}{\partial z}\left(\nu_t \frac{\partial u_2}{\partial z}\right) + F_2(z,t), \tag{45}$$

where the forcing term, $F_2(t)$ is

$$F_2(z,t) = \frac{\mathrm{d}u_\infty}{\mathrm{d}t}\,. \tag{46}$$

Assume the same series solution form of (21) and substitute into (45)

$$\sum_{n=1}^{\infty} \dot{a}_n \Psi_n = g\sum_{n=1}^{\infty} a_n (p\Psi_n{}')' + F_2(t), \tag{47}$$

where ($'$) is the derivative with respect to z and ($\dot{}$) is the derivative with respect to time.

Assume $F_2(t)$ may be represented as

$$F(z,t) = \sum_{n=1}^{\infty} F_{2_n}(t)\Psi_{2_n}(z), \tag{48}$$

and F_{2_n} is determined with

$$F_{2_n}(t) = \frac{F_2(t)}{c_{2_n}}\int_{z_o}^{d} \Psi_{2_n}(z)\,\mathrm{d}z. \tag{49}$$

Following the same procedure as given in Section 2, the complete solution of (A 1) is

$$\hat{u}_2(z,t) = \sum_{n=1}^{\infty} a_{2_n}(t)\Psi_{2_n}(z), \tag{50}$$

where

$$\Psi_{2_n} = Y_o(2\lambda_{2_n} z_o^{\frac{1}{2}}) J_o(2\lambda_{2_n} z^{\frac{1}{2}}) - J_o(2\lambda_{2_n} z_o^{\frac{1}{2}}) Y_o(2\lambda_{2_n} z^{\frac{1}{2}}),$$

and

$$a_{2_n}(t) = a_{2_n}(0)\exp^{(-\lambda_{2_n}^2 \int_0^t g(\tau)\,\mathrm{d}\tau)} + \int_0^t F_{2_n}(\sigma)\exp^{(\lambda_{2_n}^2 \int_\sigma^t g(\tau)\,\mathrm{d}\tau)}\,\mathrm{d}\sigma. \tag{51}$$

Both models use the identical shear velocity formulation as given in Section 5. The eigenvalues in second formulation are less than in formulation one, resulting in a much slower rate of decay than for that of formulation one. Also, because of the second order nature of the upper boundary condition, convergence errors may occur at large times. As such, we suggest formulation one.

References

Al-Salem, 1993. Sediment transport in oscillatory boundary layers under sheet-flow conditions. Master's Thesis, Technical University of Delft.

Baillard, J.A., 1981. An energetics total load sediment transport model for a plane sloping beach. J. Geophys. Res. 86, 2035–2043.

Beach, R.A., Sternberg, R.W., 1992. Suspended sediment transport in the surf zone: response to incident wave and long shore current interaction. Mar. Geol. 108, 275–294.

Bowen, A.J., 1980. Simple models of nearshore sedimentation; beach profiles and longshore bars. In: McCann, S.B. (Ed.), The Coastline of Canada, Paper 80-10, pp. 1–11.

Elgar, S., Guza, R.T., 1985. Observations of bispectra of shoaling surface gravity waves. J. Fluid Mech. 161, 425–448.

Elgar, S., Freilich, M.H., Guza, R.T., 1990. Model-data comparisons of moments of shoaling waves. J.Geophys. Res. 95 (C9), 16055–16063.

Fredsoe, J., Diegaard, R., 1992. Mechanics of coastal sediment transport. Advanced Series on Ocean Engineering, vol 3. World Scientific, Singapore.

Grant, W., Madsen, O.S., 1979. Combined wave and current interaction with a rough bottom. J.Geophys.Res. 84 (C4), 1797–1808.

Guza, R.T., Thornton, E.B., 1980. Local and shoaled comparisons of sea surface elevations, pressures and velocities. J. Geophys. Res. 85, 1524–1530.

Jenson, B.L., Sumer, B.M., Fredsoe, J., 1989. Turbulent oscillatory boundary layers at high Reynolds numbers. J. Fluid Mech. 206, 265–297.

Jonsson, I.G., Carlsen, N.A., 1976. Experimental and theoretical investigations in an oscillatory turbulent boundary layer. J. Hydraul. Res. 14, 45–60.

Haines, J.W., Sallenger, A.S., 1994. Vertical Structure of mean cross-shore currents across a barred surf zone. J. Geophys. Res. 99 (C7), 14223–14242.

Lavelle, J.W., Mojfeld, H.O., 1983. Effects of time-varying viscosity on oscillatory turbulent channel flow. J. Geophys. Res. 88 (C12), 7607–7616.

Madsen, O.S., Wikramanayake, P.N., 1991. Simple model for turbulent wave-current bottom boundary layer flow. Contract Rep. DRP-91-1, U.S. Army Corps of Engineers, Coastal Engineering Research Center, Vicksburg, MS.

Smith, J.D., 1977. Modeling of sediment transport on continental shelves. In: Goldeberg, E.D. (Ed.), The Sea, vol. 6. Wiley, New York, pp. 539–577.

Trowbridge, J.H., Agrawal, Y.C., 1995. Glimpses of the wave boundary layer. J. Geophys. Res. 100 (C10), 20729–20744.
Trowbridge, J., Madsen, O.S., 1984. Turbulent wave boundary layers 1. Model formulation and first-order solution. J. Geophys. Res. 88 (C5), 7989–7997.
Wallace, A., Dickinson, J.M., 1972. Empirical orthogonal representation of a time series in the frequency domain, Part 1: theoretical considerations. J. Appl. Meter. 11 (6), 887–892.